Supplementary Information

Spectral Tunable Room Temperature Superfluorescence

Hanchang Huang[1,2,3,4], Hao Liu[1,3,4*], Ye Huang[1,2,3], Mingchen Li[1,2,3], Wenda Cui[1,2,3], Changqing Song[1,2,3], Zhongjie Xu[1,2,3], Tongcheng Yu[1,2,3], Chuan Guo[1,2*], Kai Han[1,2*]

[1]College of Advanced Interdisciplinary Studies, National University of Defense Technology, Changsha, 410073, China
[2]Nanhu Laser Laboratory, National University of Defense Technology, Changsha, 410073, China
[3]Hunan Provincial Key Laboratory of High Energy Laser Technology, National University of Defense Technology, Changsha, 410073, China
[4]The two authors made equal contributions and their rankings are not distinguished.

Contents

Supplementary Note 1: Sample Preparation and Characterization.....3

1. Synthesis of $NaNdF_4$ nanocrystals.....3
2. Structural and morphological characterization. 4
3. Sample preparation for optical measurements.....4

Supplementary Note 2: Experimental Setup and Measurement Conditions 5

1. Excitation sources. 5
2. Beam delivery and sample excitation.....6
3. Detection and signal collection.....6
4. Timing calibration. 7
5. Data acquisition and measurement conditions.....7

Supplementary Note 3: Derivation of the Kinetic Model and Rate Equation Modeling 8

1. Energy-level assignment and kinetic pathway identification 8
2. Semi-empirical coupled oscillator model 12
3. Trend simulation under varying excitation fluences 15
4. Pathway-dependent population dynamics and comparison with prior studies 17

Supplementary Note 4: Experimental Evidence for UC-SF 20

1. Power dependence of the UC-SF intensity 20
2. Temporal oscillations in the emission intensity 21
3. Photon bunching revealed by second-order correlation measurements 22
4. Suppression of fluorescence oscillations at reduced doping concentrations 23

Supplementary Note 5: Conceptual Implementation of Parallel Optical Logic Gates 24

1. Input and output configuration. 24
2. Time-gated logic functionality. 26
3. Experimental reproducibility and threshold stability. 29
4. Threshold calibration procedure. 30
5. Wavelength-division multiplexing for parallel computing. 30

Supplementary Note 6: Wavelength-Synthesized Color Evolution 31

References 33

Supplementary Note 1: Sample Preparation and Characterization

1. Synthesis of $NaNdF_4$ nanocrystals.

β-$NaNdF_4$ nanocrystals were synthesized using a co-precipitation method. In a typical procedure, 1 mmol of $NdCl_3 \cdot 6H_2O$ (99.9%, Alfa Aesar) was combined with 6 mL of oleic acid (90%, Sinopharm Chemical Reagent Co., Ltd) and 15 mL of 1-octadecene (90%, Sinopharm Chemical Reagent Co., Ltd) in a three-necked flask. The mixture was heated to 160 °C under argon atmosphere and maintained at this temperature for 1 h until a clear, transparent solution formed. After cooling to room temperature, a methanolic solution containing 4 mmol of NH_4F (⩾98%, Sinopharm Chemical Reagent Co., Ltd) and 2.5 mmol of NaOH (⩾98%, Sinopharm Chemical Reagent Co., Ltd) was added dropwise under vigorous stirring, and the reaction was allowed to proceed for 1 h at room temperature. The temperature was then raised to 60 °C and held for 1 h to completely remove the methanol. Following methanol evaporation, the mixture was heated to 300 °C and maintained for 1 h to facilitate crystal growth. The resulting nanocrystals were cooled to room temperature, collected by centrifugation, and washed several times with a mixture of anhydrous ethanol and cyclohexane (both from Sinopharm Chemical Reagent Co., Ltd). The purified product was redispersed in cyclohexane and stored for further use.

2. Structural and morphological characterization.

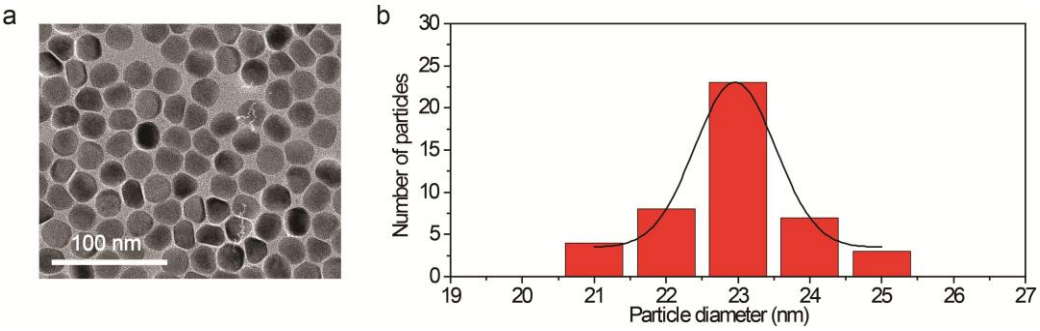

Fig.S1 Morphological characterization of the as-synthesized $NaNdF_4$ nanocrystals. (a) Representative SEM image of the $NaNdF_4$ nanocrystals. (b) Corresponding particle size distribution histogram.

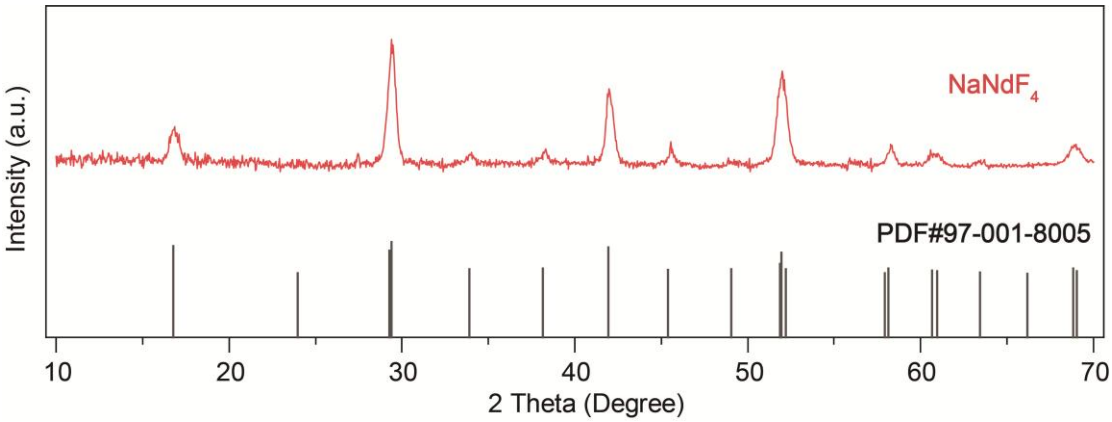

Fig.S2 Powder X-ray diffraction (XRD) patterns of $NaNdF_4$ upconversion nanoparticles (UCNPs), showing pure phase and high crystallinity of the resulting UCNPs.

Field-emission scanning electron microscope (FE-SEM, Hitachi SU8020) images revealed that the nanocrystals are approximately 23 nm in size, as shown in Fig.S1. X-ray diffraction (XRD) patterns were recorded using a Cu Kα diffractometer (Rigaku, 40 kV, 200 mA) at a scan rate of 10° min^{-1}. The diffraction data, presented in Fig.S2, confirm that the nanocrystals adopt the hexagonal β-phase structure, in agreement with the reference powder diffraction file.

3. Sample preparation for optical measurements.

For the optical experiments, 2 mL of the nanocrystal suspension at a concentration of 1 mg/mL was centrifuged at 10,000 rpm for 10 minutes. The

supernatant was discarded, and the precipitate was redispersed in 2 μL of cyclohexane. The resulting concentrated suspension was drop-cast onto a glass slide and allowed to dry, forming a deposit of aggregated particles approximately 3 mm in diameter. Only cyclohexane was used as the dispersing agent in this redispersion step.

Supplementary Note 2: Experimental Setup and Measurement Conditions

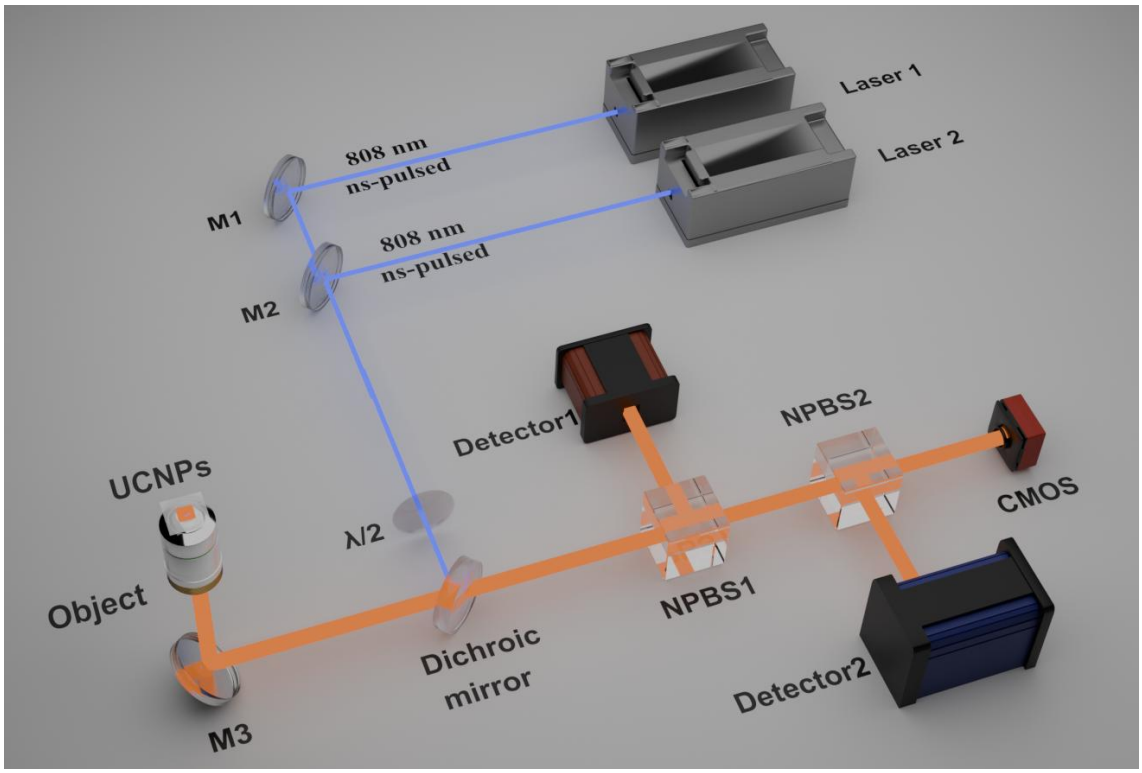

Fig.S3 Schematic diagram of the optical detection setup. The system incorporates two 808 nm nanosecond pulsed lasers (Laser 1: pulse width ~20 ns; Laser 2: pulse width ~5 ns). Key optical components include mirrors (M1, M3) and a polarization beam combiner (M2). Detection is achieved using an ICCD camera coupled to a spectrometer (Detector 1) and a PMT equipped with a monochromator and time-correlated single-photon counting module (Detector 2). The luminescence collection is equipped with an aperture diaphragm to block stray light (omitted in the illustration for clarity).

1. Excitation sources.

The optical setup employed two independently triggered 808 nm nanosecond

pulsed lasers. Both lasers were constructed by Tongfang Zhongke Chaoguang, each based on a 532 nm pulsed laser whose output was converted to 808 nm via an optical parametric oscillator (OPO) module. Laser 1 provided the light 1, which is excitation 1 (EX1) output with a pulse duration of approximately 20 ns, while Laser 2 provided Light 2, which is the excitation 2 (EX2) output with a pulse duration of approximately 5 ns. Both lasers operated at a repetition rate of 100 Hz. The output energy of the excitation light was controlled by an 808 nm attenuator (a combination of a polarizer and a half-wave plate).

2. Beam delivery and sample excitation.

The two excitation beams were combined and co-focused onto the same spot of the sample through a 100× oil-immersion objective lens (Olympus RMS100X-PFO). Spatial overlap of the excitation spots was verified by CMOS-based micro-imaging. A digital delay generator (DDG, SRS 645) was used to control the inter-pulse delay between EX1 and EX2 with nanosecond precision and to synchronize all optical detection events.

3. Detection and signal collection.

The emission from the sample was collected by the same objective and directed to three interchangeable detection modules: (i) a color CMOS camera (Thorlabs CS126CU) for wide-field imaging, (ii) an Intensified Charge-Coupled Device (ICCD, Andor istar 334) camera coupled to a spectrometer (Andor Shamrock 750) for time-resolved spectral acquisition, and (iii) a photomultiplier tube (PMT, Picoquant PMA Hybrid 40) based Time-Correlated Single Photon Counting (TCSPC, Picoquant MultiHarp 150 4P) system equipped with a monochromator (Zolix Omni-λ3027i) for high-sensitivity, wavelength-resolved lifetime measurements. Narrow bandpass filters (width less than 10 nm) were inserted in front of the detectors when isolating specific UC-SF emission bands was required.

4. Timing calibration.

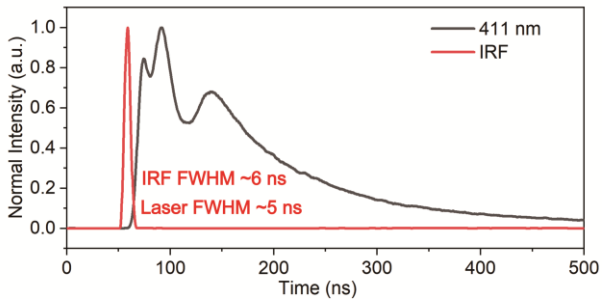

Fig.S4 Measured IRF of the detection system.

The timing of all excitation and detection events was calibrated using a fast photodiode and an oscilloscope. The DDG ensured that the ICCD gate and the PMT counting window was precisely synchronized with the laser pulses. The instrument response function (IRF) of the setup was characterized using a laser with a pulse duration of approximately 5 ns, as shown in Fig.S4. The measurement indicates that the RMS jitter of the instrument (detector and electronics) is below 2 ns.

5. Data acquisition and measurement conditions.

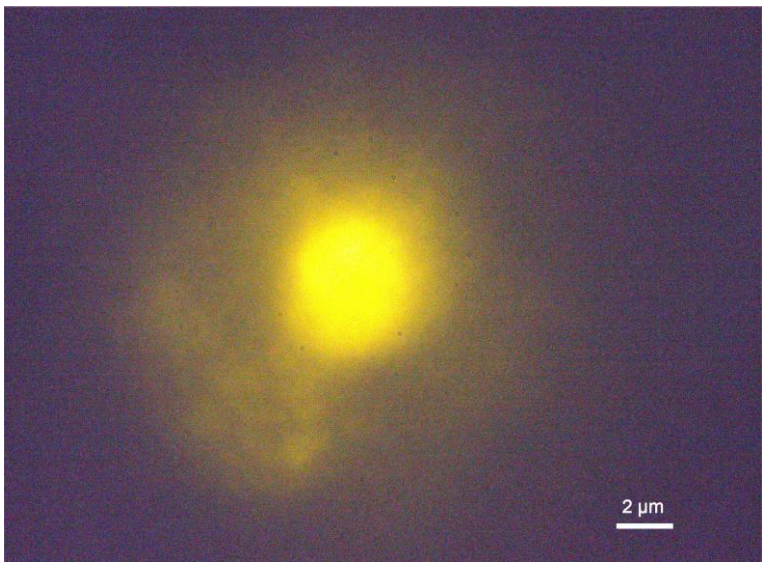

Fig.S5 Luminescence image of $NaNdF_4$ nanocrystals under 808 nm continuous-wave excitation, acquired through a microscope with a CMOS camera.

All experiments were performed at room temperature under ambient pressure. The excitation beams were focused onto the sample through a 100× oil-immersion objective lens, producing an excitation spot with a diameter of

approximately 4 μm. The sample was located using an 808 nm continuous-wave laser, as shown in Fig.S5. The pulse energies and peak irradiances used for single-pulse and dual-pulse excitation are specified in the main text and in the corresponding figure captions. All time-resolved intensity traces presented in this study were acquired using a single-photon counting PMA Hybrid detector operated in a TCSPC system. The detector exhibits a dark photon count rate on the order of 10^2/s and a saturation photon count rate of approximately 10^7/s. In all measurements reported here, the detected photon count rates lie within the range of 10^2/s to 10^4/s. A schematic of the combined EX1 and EX2 excitation configuration is shown in Fig.S6, with the inter-pulse delay denoted as t_{inter}.

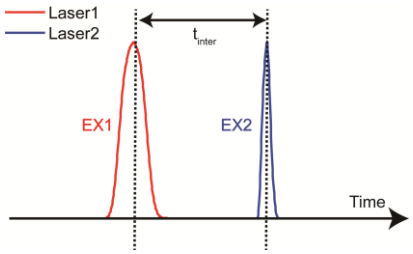

Fig.S6 Schematic illustration of the dual-pulse excitation.

Supplementary Note 3: Derivation of the Kinetic Model and Rate Equation Modeling

This note provides a comprehensive description of the kinetic model presented in Figure 3b of the main text, including the derivation of energy-level assignments, identification of dominant transition pathways, and the semi-empirical modeling framework developed to describe the multi-peak UC-SF dynamics.

1. Energy-level assignment and kinetic pathway identification

The energy-level structure depicted in Figure 3b is derived from the

well-established energy gaps of Nd^{3+} reported in References 5 (*Nat. Photon.*, 2022, 16, 737–742) and References 17 (*Nat. Commun.*, 2024, 15, 9880). These transitions represent the dominant radiative channels contributing to the observed multi-band UC-SF emission. The schematic in Figure 3b was guided by the Dicke model framework and energy conservation principles for upconversion (UC) processes. However, the specific transition pathways remain a subject of debate in the literature, with several reports proposing alternative mechanisms. Accordingly, we performed a systematic analysis by assigning each observed emission band to the complete energy-level diagram of Nd^{3+}.

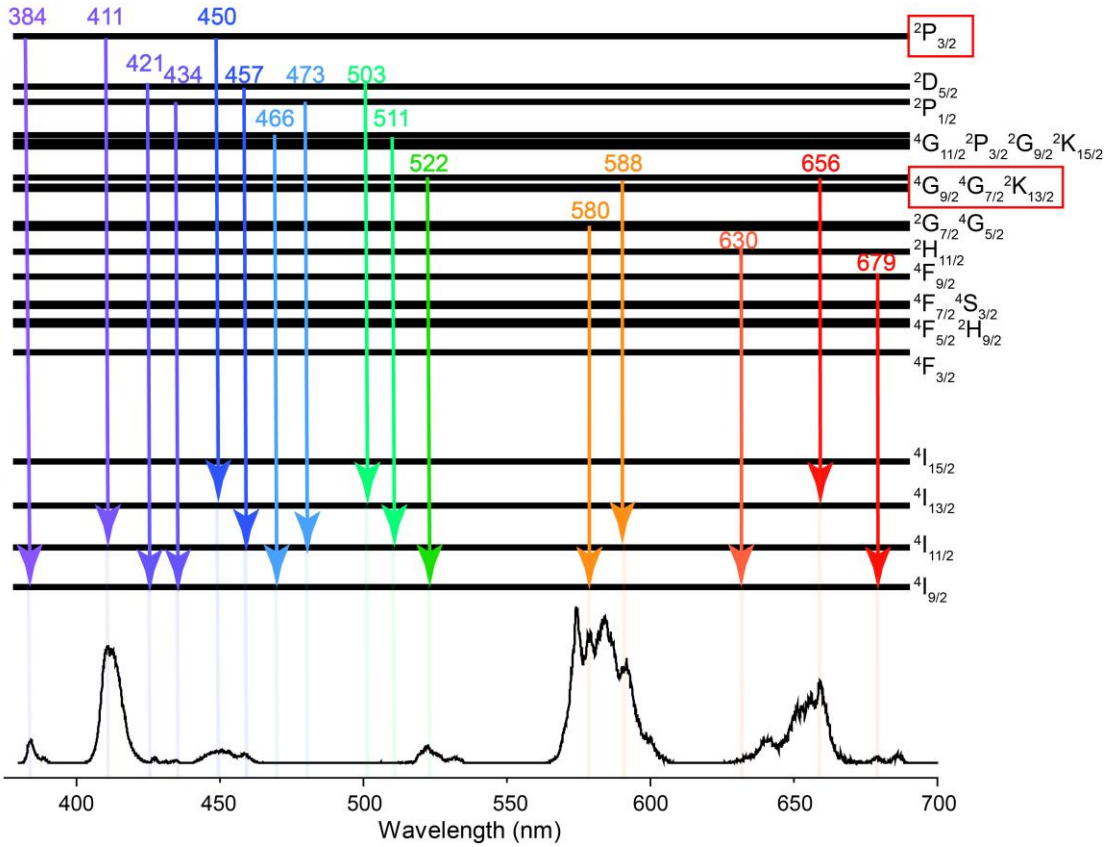

Fig.S7 Emission spectrum of $NaNdF_4$ nanocrystals recorded at a fluence of 3.6 nJ/μm² with an integration time of 1 ms, presented together with the corresponding full energy-level diagram of Nd^{3+} ions.

Based on energy-level matching considerations, we adopted the widely

recognized complete energy-level structure of Nd^{3+} and performed a systematic assignment of the observed emission bands, as illustrated in Fig.S7.[1] The results indicate that the $^2P_{3/2}$ and$^4G_{9/2}{}^4G_{7/2}{}^2K_{13/2}$ manifold constitutes the primary energy-level cluster responsible for the observed luminescence emission. This assignment is similar to the simplified energy-level schemes adopted in References 5 and 17.

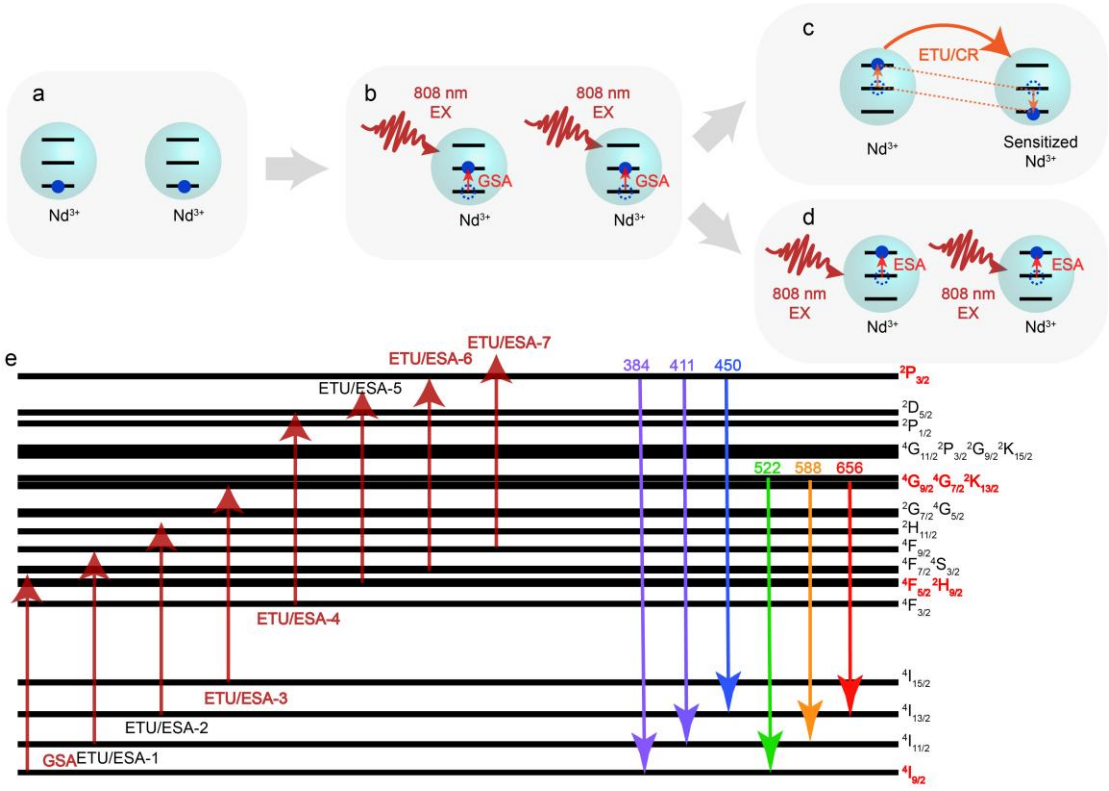

Fig.S8 (a–d) Schematic illustration of the UC process in Nd^{3+} ions. (e) Energy-level diagram illustrating UC via GSA, ESA, and ETU processes.

As shown in Fig.S8a–d, the UC process relies primarily on ground-state absorption (GSA), excited-state absorption (ESA), and energy transfer upconversion/cross-relaxation (ETU/CR) pathways to populate the upper excited states. For the GSA and ESA processes, the transition routes are fixed and coincide with the wavelength of the incident photons. By contrast, the ETU process depends on energy-level matching provided by the sensitizer ions, while the CR process relies on matching between different energy levels that already possess substantial electronic populations.

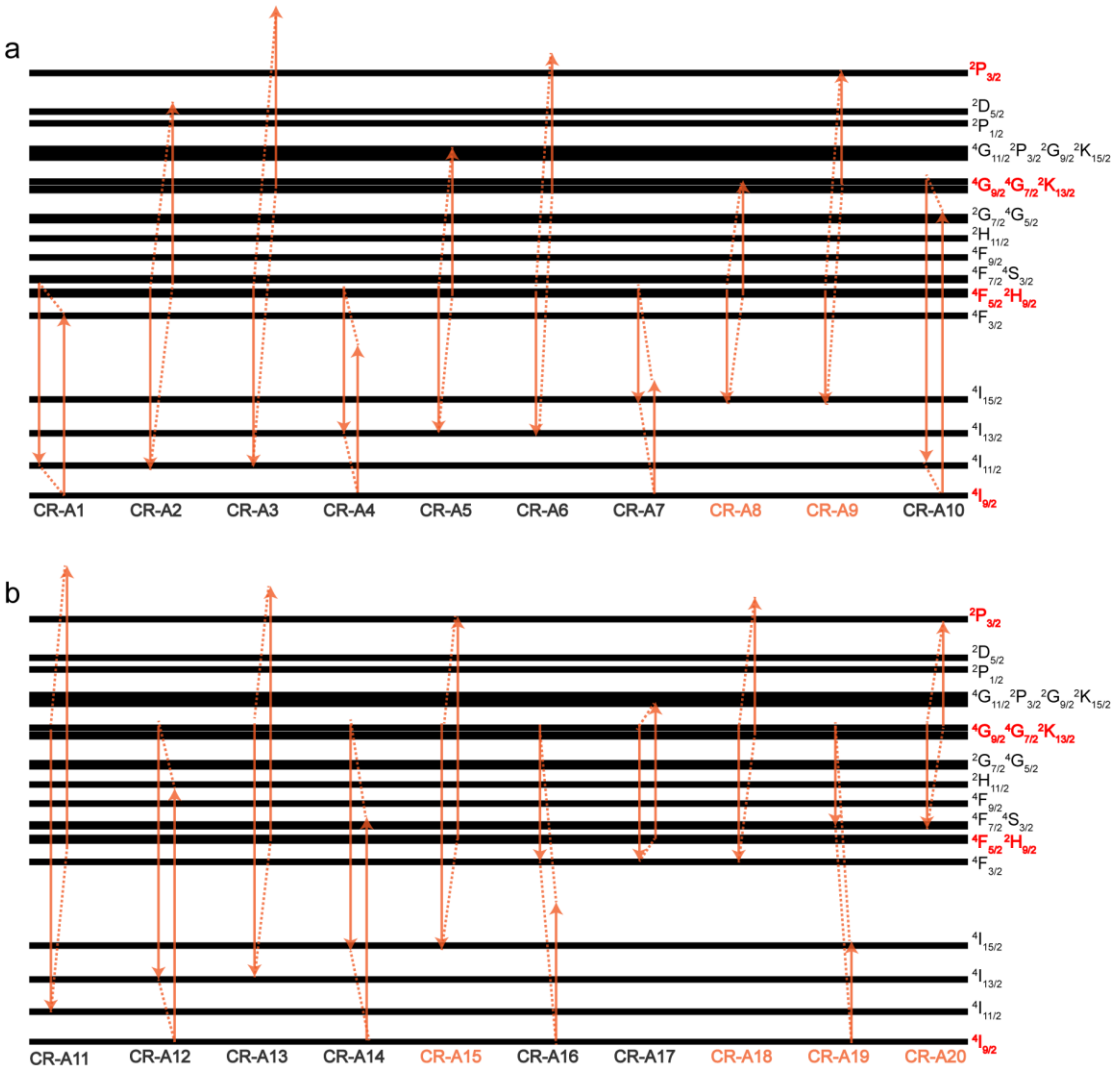

Fig.S9 Schematic illustration enumerating all possible CR pathways among Nd^{3+} ions, based on the energy levels of the prominently observed radiative transitions.

Because both the luminescent centers and the sensitizer ions in $NaNdF_4$ nanocrystals are Nd^{3+} ions and the excitation wavelength is fixed at 808 nm in this study, the GSA pathway is uniquely determined. The ETU and ESA processes also share identical energy-level matching conditions. Fig.S9e illustrates the GSA process and the possible ETU/ESA pathways. Based on the high-population energy-level cluster identified from the preceding spectral analysis and the chosen excitation wavelength, the ETU/ESA-3 and ETU/ESA-6 pathways enable efficient population accumulation and produce pronounced radiative transitions.

For CR to occur, both energy-level matching and a sufficiently high electronic

population must be satisfied simultaneously. Based on the high-population energy-level cluster and the lower-lying cluster populated by the effective ETU/ESA processes, we enumerate all possible CR pathways in Fig.S9. Among these, the CR-A8, CR-A9, CR-A15, CR-A18, CR-A19, and CR-A20 pathways satisfy the conditions for efficient population redistribution and contribute to the experimentally identified radiative transitions.

It should be noted that the above analysis is based on the effectively observed radiative transitions in the emission spectra. This does not imply that other kinetic pathways are absent. Given the complex energy-level structure of Nd^{3+} ions, the population of even higher-lying states under intense optical excitation, and the nonlinear variation of energy transfer coefficients under strong irradiation, it is impractical to incorporate all possible transition pathways into a single rate-equation simulation.

2. Semi-empirical coupled oscillator model

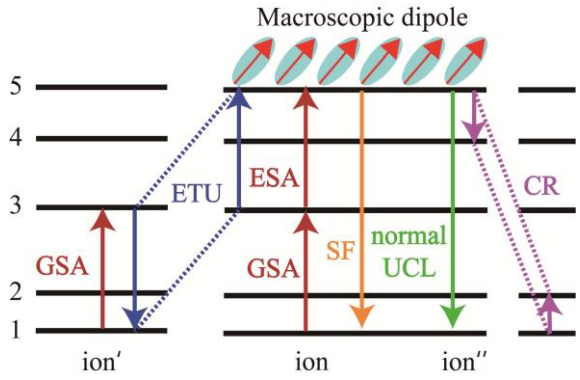

Fig.S10 A semi-empirical coupled oscillator model in combination with simplified rate equations.

We acknowledge that constructing a complete, analytically solvable rate-equation model for the full multi-stage UC-SF dynamics is challenging, owing to the large number of unknown parameters (e.g., inter-ion distances, exact ETU/CR rates, dipole–dipole coupling strengths) and the highly nonlinear, cooperative nature of SF, which involves spatiotemporal-dependent correlation effects not captured by conventional rate equations alone.

Nevertheless, to provide a more quantitative interpretation of the oscillatory dynamics, we developed a semi-empirical coupled oscillator model in combination with simplified rate equations. This approach allows us to describe the temporal competition between ESA and ETU/CR pathways and to relate the observed multi-peak structure to the population kinetics.

As illustrated in Fig.S10, the complex UC process can be deconstructed into several constituent mechanisms, including GSA, ESA, ETU, CR, conventional UCL, and SF. The dynamics of this process can be described by the following set of rate equations:

$$\frac{dn_3^{'}}{dt} = \sigma_{GSA} * E_{laser}(t) * n_1^{'} - k_{ETU} * n_3^{'} * n_3 \tag{1.1}$$

$$\frac{dn_1^{'}}{dt} = -\frac{dn_3^{'}}{dt} \tag{1.2}$$

$$\frac{dn_5}{dt} = \sigma_{ESA} * E_{laser}(t) * n_3 + k_{ETU} * n_3^{'} * n_3 - W_{UCL} * n_5 - \eta * \frac{I_{SF}(t)}{E_{photon}} - k_{CR} * n_5 * n_1 - W_{NR} * n_5 \tag{1.3}$$

$$\frac{dn_4}{dt} = k_{CR} * n_5 * n_1 \tag{1.4}$$

$$\frac{dn_3}{dt} = \sigma_{GSA} * E_{laser}(t) * n_1 - \sigma_{ESA} * E_{laser}(t) * n_3 - k_{ETU} * n_3^{'} * n_3 \tag{1.5}$$

$$\frac{dn_2}{dt} = -k_{CR} * n_5 * n_1 \tag{1.6}$$

$$\frac{dn_1}{dt} = -\frac{dn_2}{dt} - \frac{dn_3}{dt} - \frac{dn_4}{dt} - \frac{dn_5}{dt} \tag{1.7}$$

where k_{ETU} denotes the ETU rate coefficient, k_{CR} represents the CR rate coefficient, W_{UCL} is the radiative emission rate of conventional UCL, I_{SF} corresponds to the SF emission intensity, E_{photon} is the photon energy of the

SF emission, η accounts for the quantum efficiency of the SF generation, and W_{NR} accounts for the non-radiative transition rate. Additionally, σ_{GSA} and σ_{ESA} denote the absorption cross-sections for the ground state and excited state, respectively, and $E_{laser}(t)$ represents the photon number density of the excitation laser field.

Furthermore, the macroscopic dipole moment arising from the electronic population accumulated in the upper energy levels satisfies the following oscillation equation under the influence of cooperative spontaneous emission[2]:

$$\frac{\partial^2\varphi(t)}{\partial t^2}+(k+\frac{1}{2T})*\frac{d\varphi(t)}{dt}-\frac{1}{\tau^2}*e^{-\frac{t}{T}}*\sin\varphi(t)=0 \tag{1.8}$$

$$I_{SF}(\mathrm{t})=\frac{kv}{2g_0^2}*(\frac{d\varphi(t)}{dt})^2*e^{\frac{t}{T}} \tag{1.9}$$

$$\tau^2=g_0^2N(t)/v \tag{1.10}$$

$$\varphi(0)=(2/N)^{1/2},\frac{d\varphi}{dt}(0)=0 \tag{1.11}$$

where $\varphi(t)$ denotes the Bloch angle introduced through the oscillation equation and satisfies the initial condition given by Eq. (1.11). N(t) represents the number of macroscopic dipoles participating in the SF oscillatory process.

Under the assumption that all electronic population residing in the upper energy levels contributes to the formation of macroscopic dipoles, we obtain the following relation:

$$N(t)=n_5(t) \tag{1.12}$$

By solving the coupled system described by Eqs. (1.1) – (1.12), the temporal evolution of UC-SF can be obtained. When the population *N* of macroscopic dipoles is small, the number of coherently coupled emitters is insufficient to

establish robust phase correlation, and the system exhibits behavior characteristic of ordinary spontaneous UCL. As the transient population *N* gradually increases, the onset of fluorescence oscillations becomes discernible. When the instantaneous number of macroscopic dipoles *N* reaches a sufficiently high level, the emission manifests pronounced multi-stage oscillations, accompanied by a distinctive intensity profile wherein the first emission peak exhibits a lower intensity than the subsequent second peak.

3. Trend simulation under varying excitation fluences

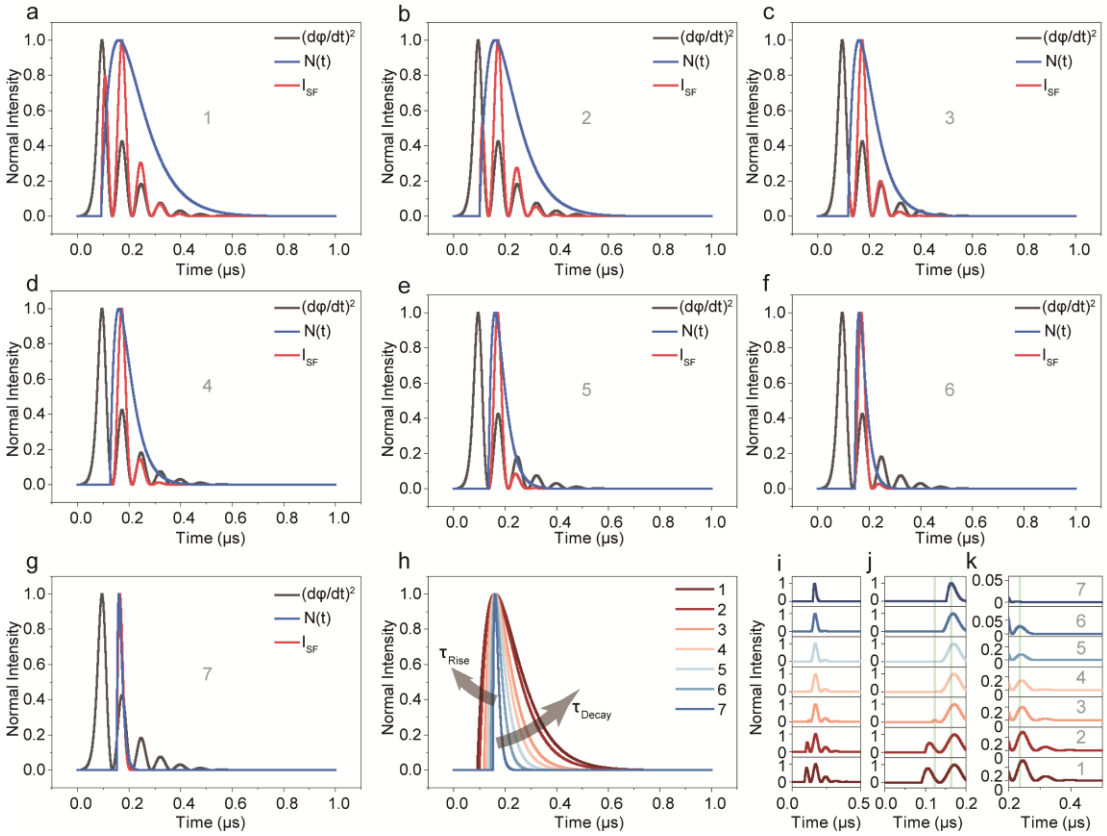

Fig.S11 (a–g) Simulated SF oscillations under different excitation power densities, showing how the evolution of the dipole population *N*(t) shapes the resulting SF emission. (h) Evolution of *N*(t) under various excitation power densities, which are numbered 1 through 7 and correspond to progressively decreasing fluence. (i) Comparison of the SF temporal profiles obtained with different *N*(t) evolutions. (j) Enlarged view comparing the first and second SF peaks. (k) Enlarged view comparing the first and third SF peaks.

We performed trend simulations of the UC-SF emission process by tracking

the temporal evolution of the population *N(t)* under seven different excitation fluences. We assumed that the system remains in a superradiant oscillatory regime with a fixed cooperation time. Fig.S11a–g display the resulting UC-SF signals for different *N(t)* profiles while the oscillation characteristics are held constant.

As shown in Fig.S11h, we present the temporal evolution of the population *N(t)* for seven different scenarios. Owing to energy migration (EM) processes, previous studies on the power dependence of UCL have consistently shown that with increasing excitation power density, the UCL rise time becomes shorter and the luminescence lifetime increases.[3] For non-superfluorescence systems, the UCL of rare-earth ions is commonly described using rate-equation models, in which the emission intensity I_{UCL} is proportional to W_{UCL}**N(t)*, where W_{UCL} denotes the radiative transition rate. On the basis of this framework, the variation of the excited-state population under different excitation power densities can be represented by the temporal evolution of *N(t)*.

By combining this relationship with the SF oscillation equation, the trend of UC-SF evolution under different excitation power densities is obtained, as illustrated in Fig.S11i. The results demonstrate that with increasing excitation power density, the UC-SF profile evolves from a single peak to double-peak oscillations and eventually to triple-peak oscillations. Notably, when multi-peak oscillations involving three or more peaks occur, the intensity of the first peak is consistently lower than that of the second peak. This behavior has not been observed in conventional SF[4–7]. This behavior is consistent with the experimental observations shown in Figure 3c–h and Figure 4a of the main text. Further comparison of the temporal characteristics of the oscillation peaks under different excitation powers reveals that as the power density increases, the first peak gradually shifts to earlier times, whereas the second and third

peaks progressively shift to later times (as shown in Fig.S11j-k). These findings are also in agreement with the experimental data acquired in this study, as presented in Figure 3c–h and Figure 4a.

4. Pathway-dependent population dynamics and comparison with prior studies

In the UC process, high-lying electronic states are populated through ESA and ETU/CR pathways, which operate on distinct timescales. The ESA process occurs almost instantaneously upon laser irradiation, on a femtosecond to picosecond timescale, whereas the ETU/CR process relies on spatial energy migration and typically proceeds on a nanosecond timescale. This difference leads to distinct population accumulation rates and influences the rising edge of the excited-state population.

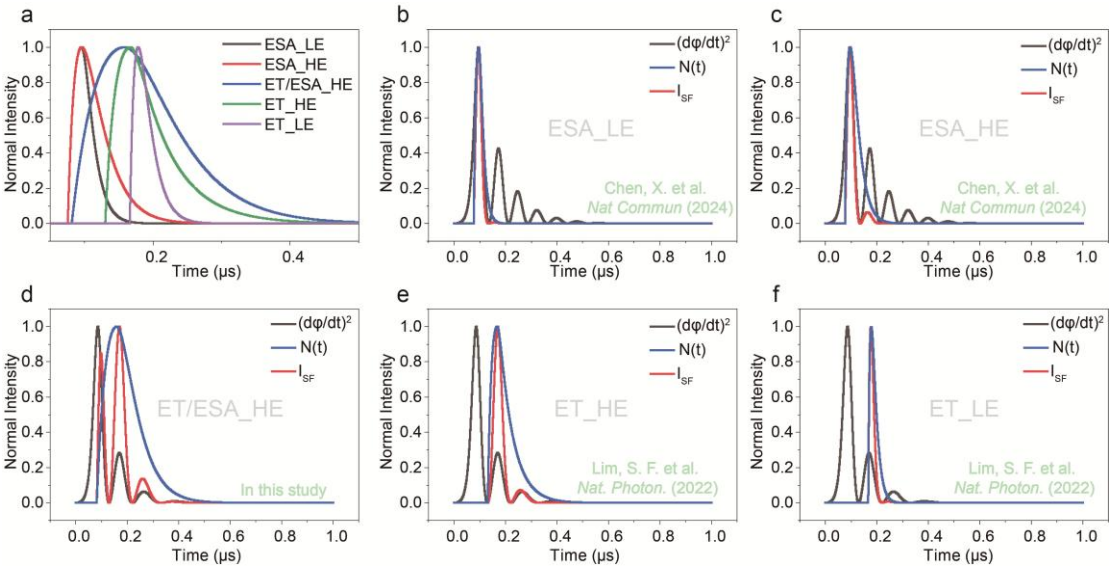

Fig.S12 (a) Temporal evolution of the electronic population *N(t)* under different dominant kinetic pathways. The black curve represents *N(t)* under low-energy excitation dominated by excited-state absorption (ESA_LE). The red curve represents *N(t)* under high-energy excitation dominated by excited-state absorption (ESA_HE). The blue curve represents *N(t)* under high-energy excitation co-dominated by energy transfer and excited-state absorption (ETU/ESA_HE). The green curve represents *N(t)* under high-energy excitation dominated by energy transfer (ETU_HE). The purple curve represents *N(t)* under low-energy excitation dominated by energy transfer (ETU_LE). (b) Oscillation

equation, *N(t)* evolution, and SF temporal profile for the ESA_LE-dominated regime. (c) Oscillation equation, *N(t)* evolution, and SF temporal profile for the ESA_HE-dominated regime. (d) Oscillation equation, *N(t)* evolution, and SF temporal profile for the ETU/ESA_HE-dominated regime. (e) Oscillation equation, *N(t)* evolution, and SF temporal profile for the ETU/ESA_HE-dominated regime. (f) Oscillation equation, *N(t)* evolution, and SF temporal profile for the ETU/ESA_LE-dominated regime.

The ESA process generally requires extremely high peak irradiance. In Reference 17 (*Nat. Commun.*, 2024, 15, 9880), femtosecond pulses were employed to achieve high peak irradiance; however, the ultrashort pulse duration results in a very small total energy per pulse. This leads to a rapid rise followed by a rapid decay of the excited-state electronic population, as illustrated by the black curve in Fig.S12a. As the femtosecond pulse energy increases, the population grows and the subsequent decay becomes relatively slower, as shown by the red curve in Fig.S12a.

By contrast, the nanosecond pulse excitation used in Reference 5 (*Nat. Photon.*, 2022, 16, 737–742) delivers a considerably lower peak irradiance compared to femtosecond excitation, but the energy per pulse is relatively higher. Under these conditions, the UC process is dominated by ETU/CR pathways, which give rise to a more gradual accumulation of the excited-state population. At low excitation energies, the population buildup is slow and the decay is relatively fast, corresponding to the purple curve in Fig.S12a. With increasing excitation energy, greater energy deposition accelerates the population buildup and slows the decay, as represented by the green curve in Fig.S12a.

In the present study, we also employ nanosecond pulses, but both the peak irradiance and the energy density per pulse significantly exceed the excitation conditions used in Reference 5. By raising the excitation power density, we achieve a peak irradiance approaching that of the femtosecond pulses in Reference 17, while the total energy density surpasses that of Reference 5.

The resulting population evolution, depicted by the blue curve in Fig.S12a, lies between the ESA-dominated and ETU/CR-dominated regimes.

Assuming a fixed cooperation number and oscillatory dynamics, Fig.S12b-c successfully reproduce the UC-SF temporal profiles reported in Reference 17, while Fig.S12e-f reproduce those of Reference 5. Notably, Fig.S12d captures the UC-SF behavior observed in our experiments, successfully reproducing the distinctive feature in which the intensity of the first SF peak is lower than that of the second SF peak.

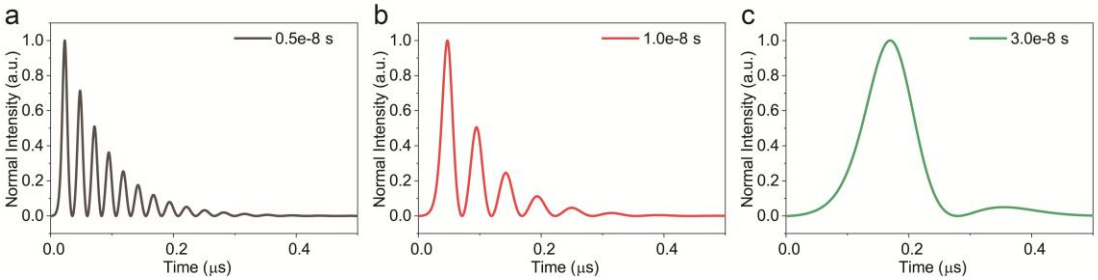

Fig. S13 Trend solutions of the oscillation equation under different cooperation times.

Furthermore, in the simulations described above, we assumed a fixed cooperation time. In actual SF dynamics, the fluorescence oscillations are closely coupled to the cooperation time: a larger number of effectively participating ions results in a shorter cooperation time. Fig.S13 illustrates the trend of the solutions to the oscillation equation under different cooperation times. Consequently, the late stage of the fluorescence decay reflects oscillatory behavior arising from a reduced number of cooperating macroscopic dipoles and the corresponding weakening of their mutual correlation. As the emission progresses into the later oscillatory regime, macroscopic dipoles persist, but their mutual correlation weakens. This reduces the number of dipoles that effectively participate in the cooperative process, which in turn lengthens the cooperation time and increases the oscillation period.

Supplementary Note 4: Experimental Evidence for UC-SF

This note compiles the key experimental evidence that establishes the SF nature of the observed UC emission in $NaNdF_4$ nanocrystals.

1. Power dependence of the UC-SF intensity

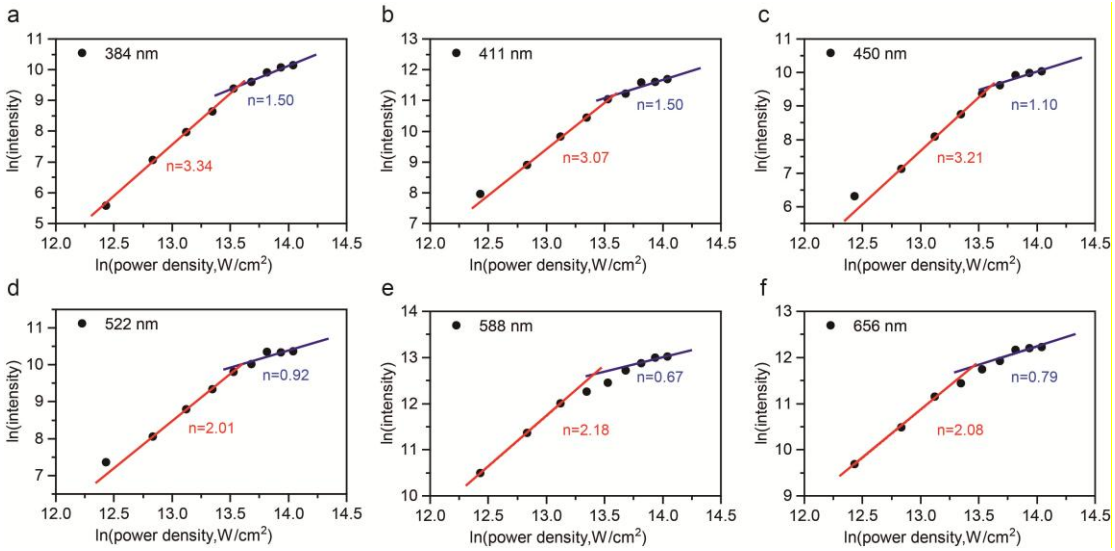

Fig.S14 Luminescence intensity as a function of excitation power density measured at different emission wavelengths.

As shown in Fig.S14, we investigated the variation of luminescence intensity with excitation power density both before and after the onset of saturation. For conventional UCL, the power-law exponent *n* is typically less than 2 for two-photon processes and less than 3 for three-photon processes due to energy losses. In the case of UC-SF, the corresponding *n* values fall within the range of 2 to 4 for two-photon processes and 3 to 9 for three-photon processes. Our experimental results demonstrate that, prior to saturation, the three-photon UC processes at 384, 411, and 450 nm exhibit *n* values exceeding 3 in certain power regimes. Similarly, the two-photon UC processes at 522, 583, and 659 nm also yield *n* values greater than 2. These findings provide evidence for the presence of UC-SF. Under saturation conditions, both

two-photon and three-photon processes display pronounced saturation behavior, with the saturated slopes falling below 1 for the two-photon processes and below 2 for the three-photon processes.

2. Temporal oscillations in the emission intensity

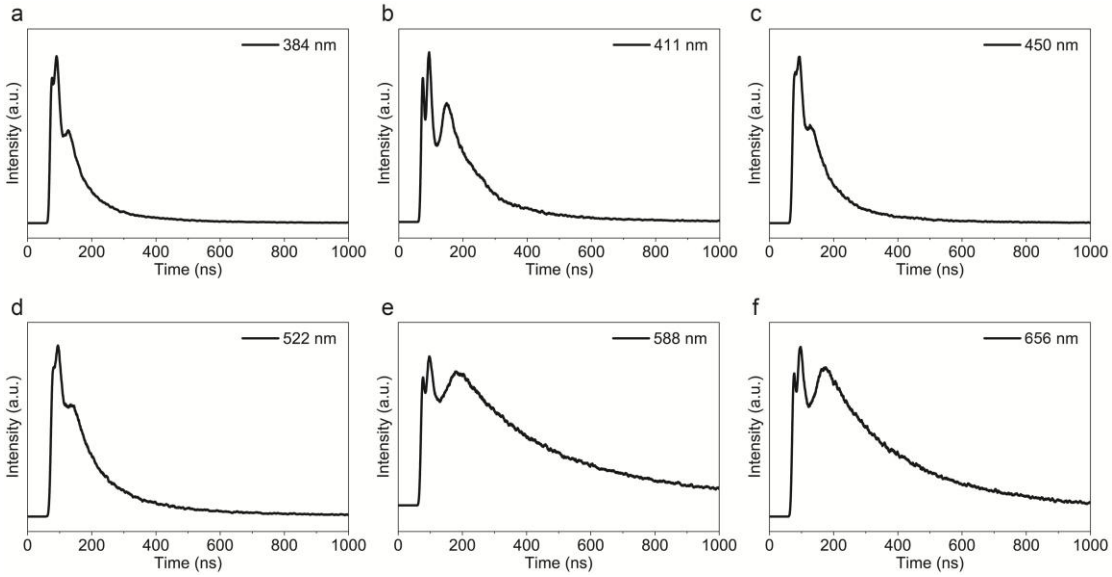

Fig.S15 Under an excitation fluence of 8.4 nJ/μm², the $NaNdF_4$ nanocrystals exhibit temporal oscillations characteristic of SF.

Distinct temporal oscillations are observed at all six emission wavelengths (384, 411, 450, 522, 588, and 659 nm), as shown in Fig.S15. At higher excitation fluences, the traces develop clear double-peak and even triple-peak structures. Such oscillatory behavior cannot be explained by independent emitters undergoing simple ESA or CR-induced quenching, which would produce a monotonically decaying signal. Instead, multi-peak oscillations are a hallmark of a cooperative radiation process in which the macroscopic dipole moment evolves coherently over time, giving rise to ringing phenomena typical of SF.

3. Photon bunching revealed by second-order correlation measurements

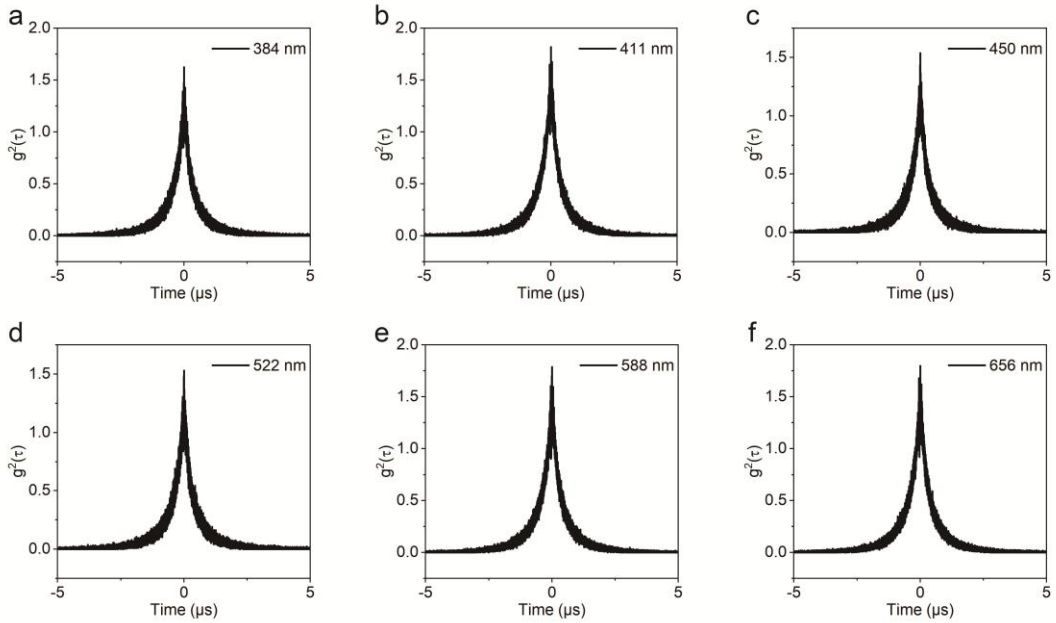

Fig.S16 Second-order correlation function g²(τ) measured for six emission wavelengths. (a) 384 nm, (b) 411 nm, (c) 450 nm, (d) 522 nm, (e) 583 nm, (f) 659 nm.

The second-order correlation function $g^2(\tau)$ was measured for each of the six UC-SF emission bands. The results are displayed in Fig.S16 of the Supporting Information. All six channels yield $g^2(0)>1$, indicating photon bunching. Photon bunching is a genuine quantum-optical hallmark of SF and arises from the cooperative emission of multiple correlated dipoles.

4. Suppression of fluorescence oscillations at reduced doping concentrations

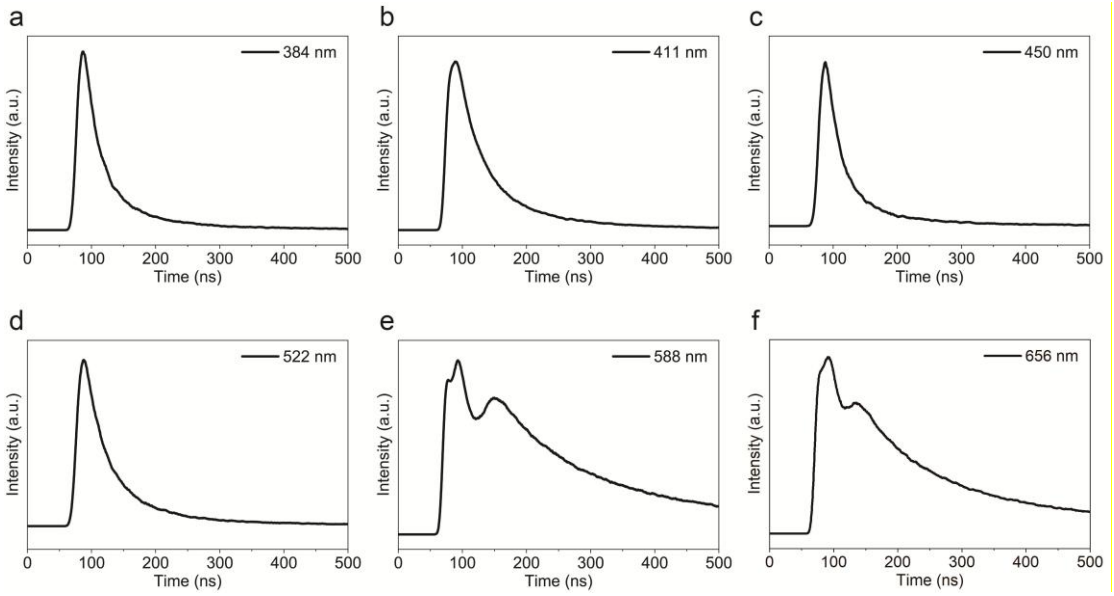

Fig.S17 Under an excitation fluence of 7.2 nJ/μm², the $NaYF_4$：Nd (70mol %) nanocrystals exhibit temporal oscillations characteristic of SF.

To further establish the cooperative origin of the observed temporal oscillations, we examined the emission dynamics of $NaYF_4$ nanocrystals with progressively lower Nd^{3+} doping levels under identical excitation conditions. In the fully doped $NaNdF_4$ sample, all six emission bands exhibit clear multi-peak oscillations, as described in Section 2. As the Nd^{3+} concentration is reduced, the oscillations become systematically weaker. At a relatively high doping concentration of 70 mol% Nd^{3+}, the intensity traces still exhibit weak oscillations (as shown in Fig.S17), yet the distinct double-peak or triple-peak structure is largely smeared out. This trend is fully consistent with the SF mechanism: in the fully doped nanocrystals, the high density of Nd^{3+} ions facilitates the formation of a large population of mutually correlated macroscopic dipoles, which is a prerequisite for collective oscillations. As the doping concentration decreases, the average inter-ion distance increases, the dipole–dipole coupling weakens, and the number of coherently coupled emitters becomes insufficient to sustain macroscopic phase correlation.

Consequently, the emission reverts to ordinary, incoherent UCL. The systematic suppression of fluorescence oscillations with decreasing doping concentration therefore provides additional evidence that the multi-peak dynamics observed in $NaNdF_4$ originate from SF rather than from single-ion processes such as excited-state absorption or cross-relaxation.

Supplementary Note 5: Conceptual Implementation of Parallel Optical Logic Gates

In this note, we provide a detailed account of the conceptual implementation of parallel optical logic gates based on UC-SF from an aggregate of $NaNdF_4$ nanocrystals. The logic operations exploit the dual-pulse excitation scheme described in the main text, where two 808 nm nanosecond laser pulses, denoted as EX1 and EX2, serve as the optical inputs. The six UC-SF emission bands centered at 384, 411, 450, 522, 588, and 659 nm function as output channels, each carrying a logic state determined by its time-gated emission intensity. All measurements were performed on a single representative aggregate spot, formed by drop-casting a suspension of ~23 nm $NaNdF_4$ nanocrystals onto a glass slide, resulting in a micron-sized, densely stacked particle assembly. While the constituent nanocrystals are individually nanometer-sized, the emission is collected from the entire micrometer-scale aggregate.

1. Input and output configuration.

EX1 is a strong primary pulse that initiates the UC-SF process and establishes the initial population and macroscopic dipole correlation. EX2 is a weak, time-delayed secondary pulse that can actively restore dipole correlation without generating a significant new excited-state population on its own. The logic state of each output channel is defined by the integrated UC-SF intensity

within a specified temporal window after the excitation sequence. A binary value of "1" is assigned when the detected intensity exceeds a preset threshold, and "0" when it falls below that threshold.

Benefiting from the newly discovered tunable UC-SF phenomenon, we demonstrated a proof-of-concept logical gate operation using nanocrystal aggregate. In the experiment, two laser beams (I_1 and I_2) served as the input signals, while distinct UCL emission wavelengths functioned as the output states, as illustrated in Fig. S18. This demonstration effectively validates the potential of our approach for future applications in optical computing. The above experiment proves that two lasers can externally regulate the spectra and intensity evolving of UC-SF over time. Therefore, the encoded nanoparticles (NPs) are used for proof-of-concept demonstration of parallel optical logic gate. We use two laser beams (I_1, I_2) as inputs and UC-SF with 6 different spectral bands as outputs. The UC-SF are observed by using narrowband filter with corresponding wavelength and a Photoelectric Detector (PD) in each parallel channel. Different laser excitation modes, such as only EX1, only EX2, or a combination of EX1 and EX2 excitation, can regulate the pathway of transitions and obtain UC-SF with different emission characteristics. The UC-SF intensity at specific moments corresponding to different excitation modes has a clear regularity, therefore, the values of 0 and 1 in the output can be represented by luminescence intensity measured by the PD at individual wavelength, and distinguished by intensity threshold. EX1 and EX2 are used as inputs at different time intervals, which can regulate different UC-SF emission patterns. At the output end, 0 and 1 values that comply with Boolean logic operations can be obtained, thus enabling the implementation of three basic types of logic gates: AND, OR, and NOT gate. It is worth emphasizing that the proposed logic gate is composed of all-optical hardware, and above experiments demonstrates that all six spectral bands of UC-SF can be

manipulated, which means that NPs as optical logic gates can achieve 6-channel optical computing. In addition, the structure of NP-based optical logic gate is simple, robust, and its micro/nanoscale size is suitable for on-chip integration. Combined with its synchronous computing characteristics, it can serve as a promising and universal platform for optical logic gate, paving the way for future high-speed optical computing and relative advanced applications.

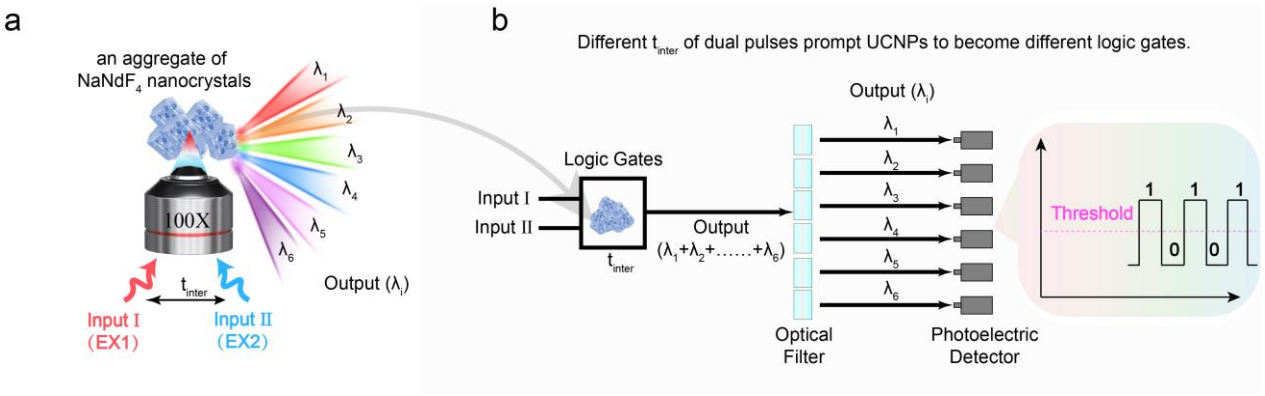

Fig.S18 Reconfigurable optical logic gates enabled by multiple spectral channels UC-SF via $NaNdF_4$ nanocrystals. (a) Schematic of multi-wavelength UC-SF emission under dual-pulse excitation. (b) Diagram of parallel optical logic gate containing up to 6 independent channels associated with 6 wavelength spectral bands. Optical inputs (I_1, I_2) are external manipulable laser pulses, and emission intensity captured by Photoelectric Detector (PD) after narrow-band filter serves as output of optical logic gate.

2. Time-gated logic functionality.

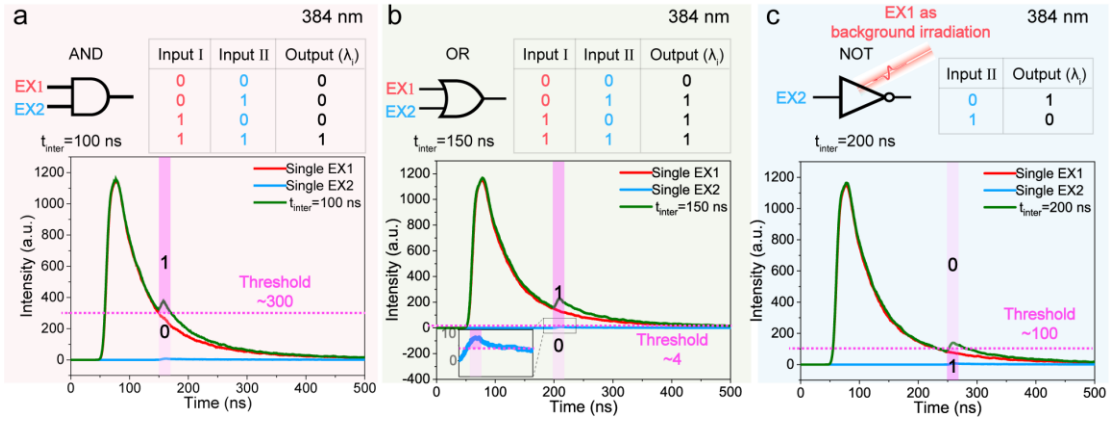

Fig.S19 (a-c) The 0 and 1 values in the output are represented by luminescence intensity at

384 nm, and distinguished by intensity threshold. The luminescence observations at different times serve as different optical logic gate functions: (a) AND, (b) OR, and (c) NOT gates.

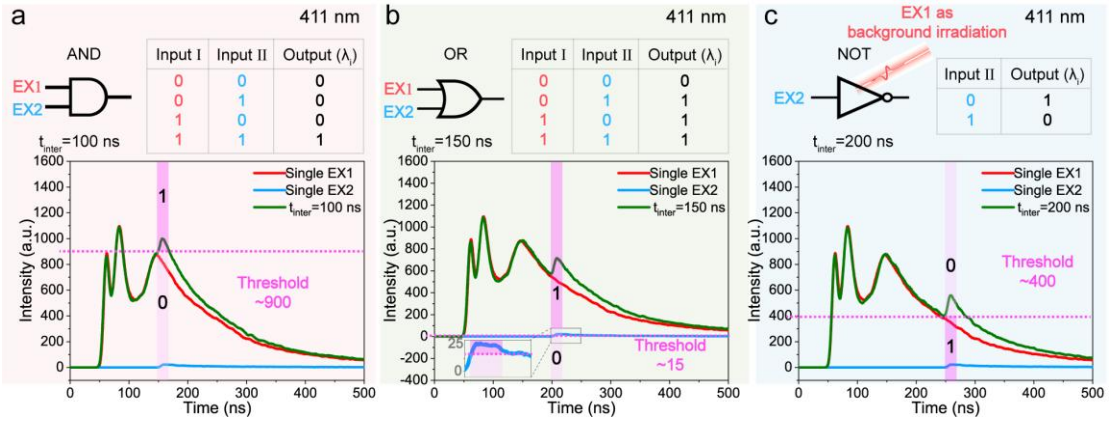

Fig.S20 (a-c) The 0 and 1 values in the output are represented by luminescence intensity at 411 nm, and distinguished by intensity threshold. The luminescence observations at different times serve as different optical logic gate functions: (a) AND, (b) OR, and (c) NOT gates.

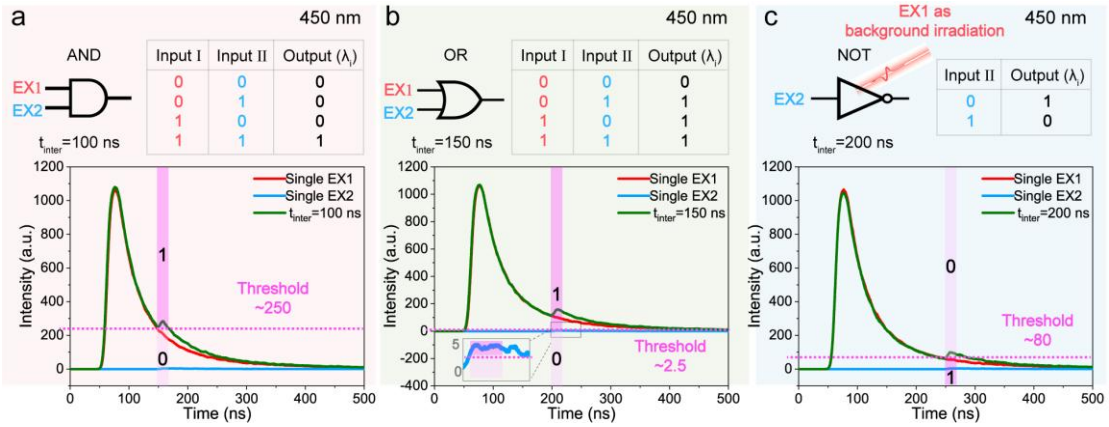

Fig.S21 (a-c) The 0 and 1 values in the output are represented by luminescence intensity at 411 nm, and distinguished by intensity threshold. The luminescence observations at different times serve as different optical logic gate functions: (a) AND, (b) OR, and (c) NOT gates.

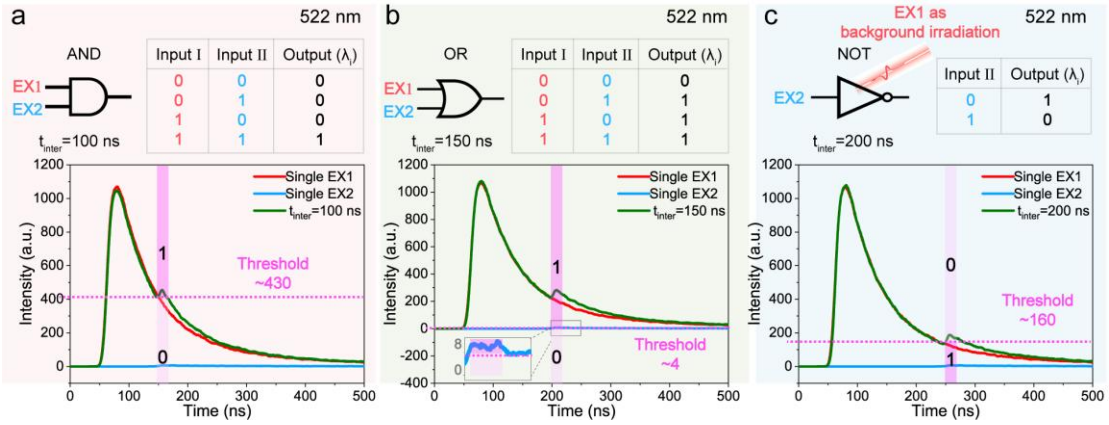

Fig.S22 (a-c) The 0 and 1 values in the output are represented by luminescence intensity at 522 nm, and distinguished by intensity threshold. The luminescence observations at different times serve as different optical logic gate functions: (a) AND, (b) OR, and (c) NOT gates.

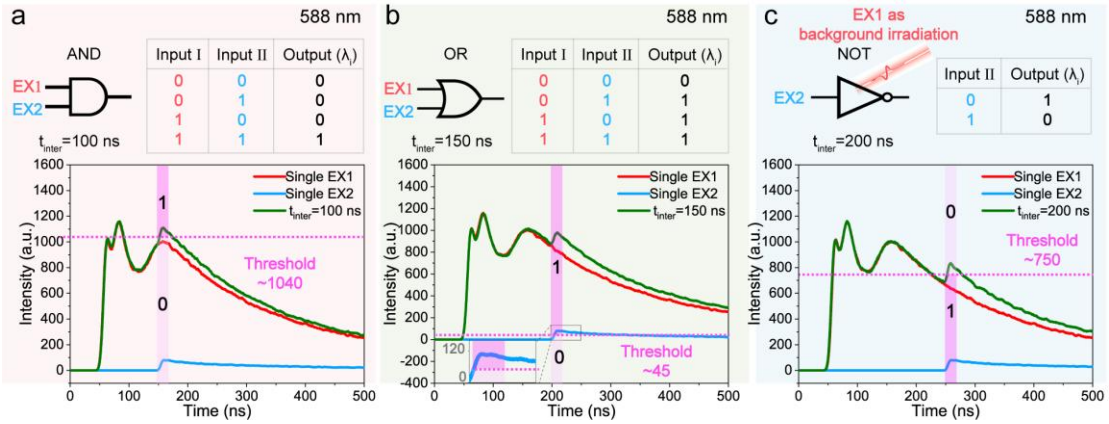

Fig.S23 (a-c) The 0 and 1 values in the output are represented by luminescence intensity at 588 nm, and distinguished by intensity threshold. The luminescence observations at different times serve as different optical logic gate functions: (a) AND, (b) OR, and (c) NOT gates.

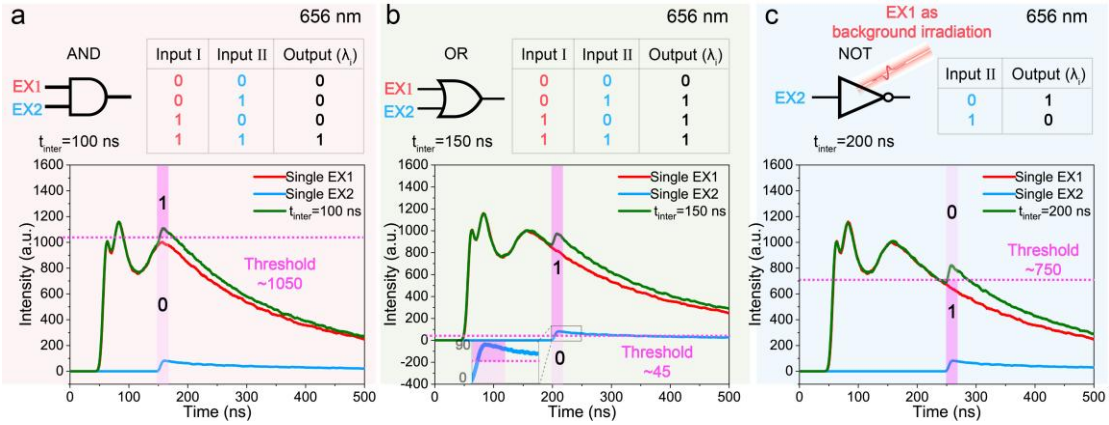

Fig.S24 (a-c) The 0 and 1 values in the output are represented by luminescence intensity at

659 nm, and distinguished by intensity threshold. The luminescence observations at different times serve as different optical logic gate functions: (a) AND, (b) OR, and (c) NOT gates.

By adjusting the inter-pulse delay of EX2 and selecting appropriate detection time windows, the same emission channel can implement different Boolean logic operations. For instance, when the detection window is placed shortly after EX2 and the EX2-induced enhancement is necessary to reach the threshold, the system behaves as an AND gate (both EX1 and EX2 required). When the detection window is positioned to capture the emission tail from EX1 alone or the enhanced signal from EX1+EX2, an OR gate is realized (either pulse sufficient). A NOT gate can be implemented by defining the "1" state as the emission from EX1 alone and "0" as the state when EX2 is applied and its re-synchronization effect alters the temporal profile, causing the intensity in a later window to drop below threshold. These three basic gate types (AND, OR, NOT) are demonstrated for all six wavelength channels, as summarized in Fig.S19, Fig.S20, Fig.S21, Fig.S22, Fig.S23 and Fig.S24.

3. Experimental reproducibility and threshold stability.

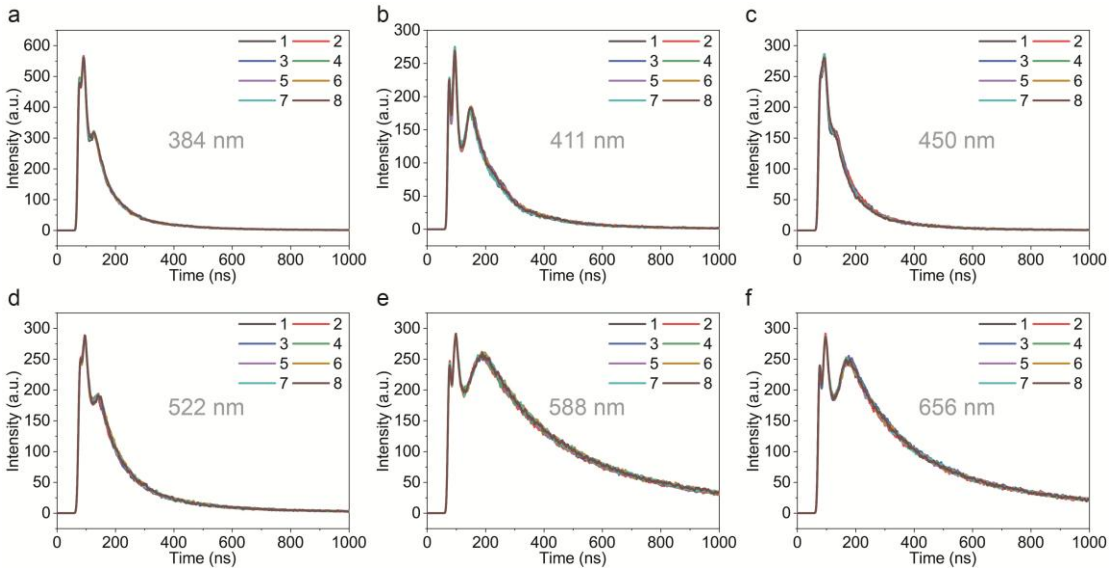

Fig.S25 Repeated measurements of the time-resolved luminescence intensity at different emission wavelengths for $NaNdF_4$ nanocrystals, recorded at a single sample position under EX1 excitation.

To verify the reliability of the logic operations, we performed eight repeated measurements of the luminescence emission at the same wavelength, at the same sample position, and under identical EX1 excitation conditions, as shown in Fig.S25. The recorded UC-SF intensity traces were highly reproducible, with intensity fluctuations confined within a narrow range. This confirms that the emission state of a given aggregate spot remains stable over multiple excitation cycles and that the binary state discrimination based on preset intensity thresholds is equally robust.

4. Threshold calibration procedure.

The intensity threshold for each logic channel is determined from the set of repeated measurements at the target sample position. The mean intensity and the standard deviation of the "low" and "high" states are extracted, and the threshold is set at a level that maximizes the discrimination margin. Due to the high stability of the emission, the calibrated threshold can be used for the same location of the same sample. This approach aligns with established practice in logic demonstrations. Universal thresholds are typically not feasible owing to variations in sample morphology and local excitation conditions, and dedicated calibration is therefore relied upon to ensure reliable functionality.

5. Wavelength-division multiplexing for parallel computing.

Since all six emission bands originate from the same aggregate and can be simultaneously detected through appropriate spectral filtering, six independent logic channels can operate in parallel. By adjusting the detection windows and threshold settings, these six channels can concurrently execute Boolean functions. This wavelength-division multiplexing approach, combined with temporal gating, effectively constitutes a multi-channel optical logic unit within a single microscopic sample region. The conceptual architecture is illustrated

in Figure 6 of the main text.

In summary, the proof-of-concept demonstration establishes that UC-SF in aggregated $NaNdF_4$ nanocrystals can serve as a versatile platform for encodable, multi-channel, time-gated optical logic operations. While the current implementation focuses on basic Boolean functions and is performed on a micron-scale particle assembly, the principles of temporal control and spectral parallelism may inform future designs of high-speed photonic computing architectures.

Supplementary Note 6: Wavelength-Synthesized Color Evolution

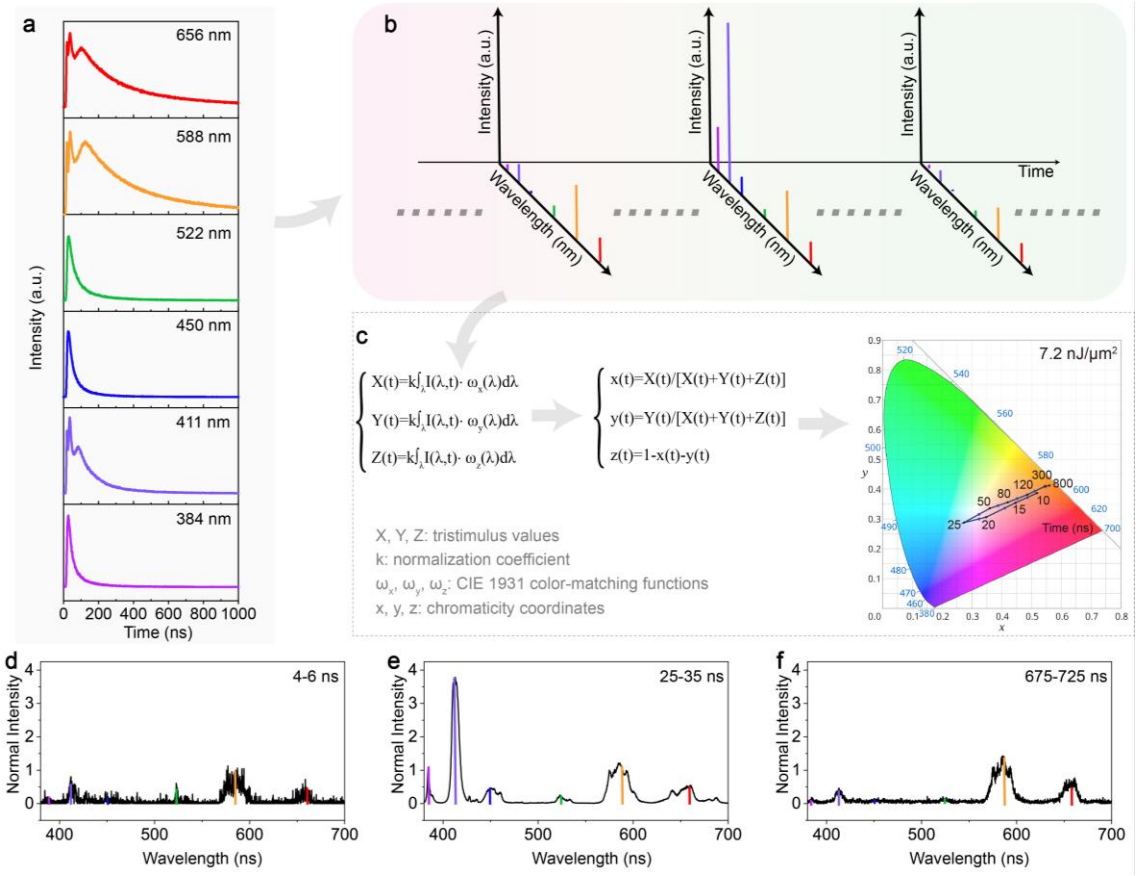

Fig.S26 Wavelength-synthesized color evolution of UC-SF. (a) Time-resolved fluorescence intensity curves of the six characteristic emission wavelengths. (b) Schematic illustration of wavelength synthesis, showing how the intensities extracted at a given instant from the lifetime curves are combined into a synthesized spectrum. (c) Color evolution trajectory calculated

from the synthesized spectra using the CIE 1931 chromaticity coordinates. (d–f) Normalized transient spectra recorded at three representative time intervals, exhibiting distinct intensity distributions among the emission wavelengths that corroborate the synthesized color evolution.

Figure S26 illustrates the wavelength-synthesized color evolution process for the short-lived upconversion superfluorescence (UC-SF) emission. For ultrafast emission processes such as superfluorescence, the time-dependent color evolution can be reconstructed from the lifetime curves recorded at individual wavelengths rather than through steady-state spectral integration. Figure S26a presents the temporal evolution of the fluorescence intensity at the six characteristic UC-SF emission bands. From these traces, the intensities at a given instant are extracted and combined into a synthesized spectrum, as schematically shown in Fig. S26b. The wavelength-synthesized color evolution trajectory is then obtained by processing these spectra through the CIE 1931 chromaticity coordinates, as displayed in Fig. S26c.

To further validate the color synthesis approach, transient spectra were experimentally acquired over different time intervals. As shown in Figs. S26d–f, the normalized transient spectra recorded at three representative time windows clearly exhibit distinct intensity distributions among the six emission wavelengths. These variations in the relative spectral weights at different instants confirm that the color evolution trajectory derived from the lifetime curves faithfully represents the true temporal dynamics of the multi-wavelength UC-SF emission.

It is worth noting that human vision perceives color by integrating the visible spectrum over millisecond timescales, a limitation imposed by the finite temporal resolution of the eye. In conventional display technology, wide-gamut color is typically achieved by splitting white light into red, green, and blue components with color filters and controlling their relative intensities through liquid crystal modulation. Color synthesis from discrete wavelength channels is

therefore a well-established technique in color science. For ultrashort emission processes such as UC-SF, the characteristic timescale is on the order of nanoseconds, far shorter than the millisecond recognition window of the human eye. To capture color evolution on such ultrafast timescales, single-point detectors combined with bandpass filters are employed, and the complex spectral information is represented through the synthesis of multiple wavelength channels. This method is of considerable significance for applications such as high-speed color displays, laser color imaging, and spectrally encoded imaging systems.[8-10]

References

1. Carnall, W. T., Fields, P. R. & Rajnak, K. Electronic Energy Levels in the Trivalent Lanthanide Aquo Ions. I. Pr^{3+}, Nd^{3+}, Pm^{3+}, Sm^{3+}, Dy^{3+}, Ho^{3+}, Er^{3+}, and Tm^{3+}. *J. Chem. Phys.* **49**, 4424–4442 (1968).
2. Bonifacio, R. & Lugiato, L. A. Cooperative radiation processes in two-level systems: Superfluorescence. *Phys. Rev. A* (1975).
3. Han, Y. *et al.* Modulating the Rise and Decay Dynamics of Upconversion Luminescence through Controlling Excitations. *Angew Chem Int Ed* **61**, (2022).
4. Kobiyama, E. *et al.* Perovskite Nanocrystal Self-Assemblies in 3D Hollow Templates. *ACS Nano* **19**, 6748–6757 (2025).

5. Aggarwal, N. *et al.* Room Temperature Superfluorescence from an Electron-Hole Liquid. *Phys. Rev. Lett.* **134**, 083801 (2025).
6. Zhou, M. *et al.* Ultrafast upconversion superfluorescence with a sub-2.5 ns lifetime at room temperature. *Nat Commun* **15**, 9880 (2024).
7. Huang, K. *et al.* Room-temperature upconverted superfluorescence. *Nat. Photon.* **16**, 737–742 (2022).
8. Wang, X. et al. Active Hyperspectral Imaging with Wavelength-Encoded Illumination Using Perovskite Nanocrystals. *ACS Photonics* **12**, 6920–6925 (2025).
9. Park, J. & Gao, L. Cascaded compressed-sensing single-pixel camera for high-dimensional optical imaging. *PhotoniX* **5**, 37 (2024).
10. Zhu, X. et al. Broadband perovskite quantum dot spectrometer beyond human visual resolution. *Light Sci. Appl*. **9**, 73 (2020).